Check for updates

Received: 10 February 2023 | Revised: 12 April 2023 | Accepted: 2 May 2023

DOI: 10.1049/rsn2.12422

IET Radar, Sonar & Navigation

The Institution of Engineering and Technology WILEY

ORIGINAL RESEARCH

Estimation of drone intention using trajectory frequency defined in radar's measurement phase planes

Joongsup Yun[1] | David Anderson[2] | Francesco Fioranelli[3]

[1]School of Aerospace, Transport and Manufacturing, Cranfield University, Cranfield, UK

[2]School of Engineering, University of Glasgow, Glasgow, UK

[3]Microwave Sensing Signals & Systems Group, Delft University of Technology, Delft, The Netherlands

Correspondence

Joongsup Yun.
Email: joongsup.yun@gmail.com

Funding information

Office of Naval Research Global, Grant/Award Number: N62909-19-1-2073

Abstract

This paper presents a radar-based algorithm for autonomous estimation of drone intention. The algorithm is based on radar's kinematic measurements, providing fast and robust intention estimation for multiple targets. The core idea of the proposed algorithm is to build intention-specific features for each intention in advance and use them in actual drone surveillance situations. To effectively depict the trajectory characteristics of various intentions, the trajectory frequency is computed on multiple phase planes through Monte Carlo Simulations. Finally, a naive Bayes classifier is applied to integrate the trajectory likelihood in different phases and ultimately compute the intention likelihood of all intentions concerned. Numerical simulations for the three candidate intentions of image acquisition, smuggling, and kamikaze attack demonstrated the performance of the presented method. The simulation results show that one can estimate the true intention of a specific drone by comparing the value of each intention likelihood.

KEYWORDS

Bayes methods, pattern classification, radar target recognition, radar tracking, statistical analysis

1 | INTRODUCTION

In recent years, the number of incidents caused by drone swarms has increased. For an effective response to drone swarms, C-UAS (Counter Unmanned Aircraft System) systems are being equipped with automated processes that provide decision makers with accurate and low-latency target information. Figure 1a shows the processing chain of a typical C-UAS system where the degree of autonomy varies for each task. Task 1 (detection, tracking) in a typical surveillance system is fully automated. In contrast, Tasks 2 (identification, classification), 3 (behaviour analysis, intention estimation), and 4 (decision-making) still require human involvement at some level [1].

This paper presents a radar-based algorithm for autonomous estimation of drone intention. The algorithm is divided mainly into the pre-processing phase and the intention estimation phase. The pre-processing phase aims to establish an *Asset-Dependent Intention Bank* (*ADIB*) based on the drone mission model. ADIB is composed of statistical features that characterise typical trajectory patterns for the intentions considered. This paper proposes the trajectory frequency as the main statistical feature that is obtained from Monte Carlo simulations. On the other hand, the intention estimation phase aims to calculate the likelihood of each intention in the ADIB using the naive Bayes approach.

The trajectory frequency is computed using radar kinematic measurements, namely the estimated position and velocity of different detected drones. The usefulness of intention estimation capabilities based on radar data can be clearly understood through the following example. Suppose a drone breached a geofence around a military installation and is being tracked by a drone surveillance system. An EO/IR (Electro-Optical and Infra-Red) system will capture an image of the drone and show it to the human operator. If the human operator discovers from the image that the drone is carrying explosives, it can be confirmed that the drone has the intent of 'bombing' [2]. Even if autonomous image recognition technologies are applied, this approach of estimating intent is not appropriate for the case where numerous drones are simultaneously present in the surveillance area. This is because most

This is an open access article under the terms of the Creative Commons Attribution-NonCommercial-NoDerivs License, which permits use and distribution in any medium, provided the original work is properly cited, the use is non-commercial and no modifications or adaptations are made.

© 2023 The Authors. *IET Radar, Sonar & Navigation* published by John Wiley & Sons Ltd on behalf of The Institution of Engineering and Technology.

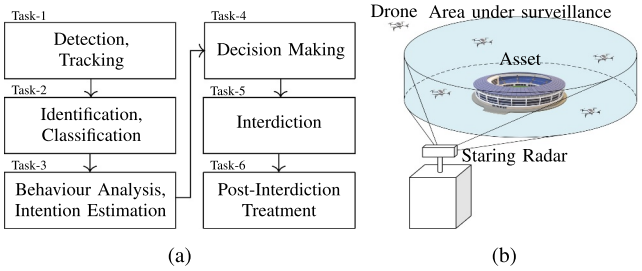

FIGURE 1 (a) Processing chain of the conventional C-UAS system, (b) Drone surveillance system based on staring radar.

EO/IR systems typically have a small instantaneous field of view (IFoV), meaning that a very limited number of targets can be simultaneously tracked. On the contrary, radars have a wider coverage of both range and direction, which means that they can track multiple drones at the same time. Moreover, radar can be operated in all weather conditions.

Among the various types of radar system, this paper considers staring Frequency-Modulated Continuous-Wave (FMCW) radar as the primary sensing technology. Staring radars are usually adopted in C-UAS systems because they have advantageous performance benefits compared to scanning radars in drone surveillance applications [3, 4]. Staring radars often have a long Coherent Processing Interval (CPI), which is essential to detect slow-moving multi-copters and their Doppler signatures with fine resolution. Figure 1b illustrates a counter-UAS scenario where a staring radar is the main sensor system and unidentified drone swarms are surrounding a stadium, for example, in case of a public event.

1.1 | Related work

The three recurring keywords in studies related to intention estimation (that is, Task-3 in Figure 1a) are anomaly detection [5–7], threat assessment [8], and intent inference [9–13]. Among references dealing with intent inference, we review [9–11] first in which the targets considered are drones.

Ref. [9] proposed an algorithm to estimate the malicious intent of a drone. The algorithm is based on a Bayesian inference approach and uses radar data as its sensor system. However, their concept of intent appeared to be defined to refer only to a drone's tendency to enter or remain in a particular portion of the airspace, such as no-fly zones. No further considerations as to velocity or flying patterns were used to inform a more detailed assessment of the intent, such as the purpose of the flight.

Ref. [10] analysed micro-Doppler data of a drone modified to carry and release a grenade. The author showed that the micro-Doppler HERM (HElicopter Rotor Modulations) lines of the drone vary depending on whether the drone is still carrying or has released the grenade. This idea could be used to determine if a drone has a 'bombing' intention, but it would not be easily applicable to scenarios of low SNR or long distance, where the signature of the blades is undetectable.

Ref. [11] proposed an RF-based drone detection and identification method. The key idea of this study is that every drone platform emits different RF patterns from one platform to another. If a drone is recording a video and transmitting it to a ground station, it generates unique RF patterns. Although interesting for the potential passive detection and analysis of these RF emissions, this approach would not be easily applicable at long distances and for drones that are highly autonomous and do not communicate with a ground station.

Refs. [12, 13] proposed radar-based integrated intent inference and tracking filter algorithms. The targets considered in these references are ground vehicles and manned aircraft, respectively. In such algorithms, the performance of the tracking filter is expected to be enhanced by using the inferred intent of the tracked objects.

Ref. [12] proposed the autonomous spatial pattern estimation method for a ground target. Spatial patterns that can be estimated include a line, arc, or rectangle, which are then fed to the tracking filter. In other words, the target intent in the paper is defined as the intention to maintain a certain trajectory pattern. This means that higher-level intentions must be estimated by human operators.

Ref. [13], on the other hand, proposed a method that can simultaneously estimate the class and intent of a military manned aircraft. The considered classes are cargo and fighter, and the considered intents are cruise and attack. The paper demonstrated the performance of the proposed algorithm through numerical simulations. Meanwhile, a limitation of the proposed method is that the intention estimation is highly correlated with only the acceleration estimation. In other words, targets with high acceleration are considered to have a high probability of attack intent. Taking into account these modelling characteristics, their proposed method is not always appropriate to model intent which should be described also in relation to other targets or assets in the scenario. For example, the target A's intent of chasing target B, or flying along a circular trajectory around asset C, cannot be modelled by using acceleration-only approaches. The acceleration-based intention estimation of fixed-wing manned aircraft cannot be directly applied to small drones because they, especially multi-copters, can perform more agile manoeuvres than manned aircraft. In other words, in the case of small drones, the dynamic range of the acceleration can be quite large regardless of the drone's mission.

1.2 | Main contributions

The main contribution of this paper is that it presents a novel methodology for estimating drone intention using radar's kinematic measurements, where the term 'intention' indicates the specific mission or the purpose of the drone's flight. As mentioned in Section 1.1, the definitions of the intention of a target differ in the different related studies. Among the various definitions of intent, the mission or the purpose of the flight is the highest level of intention that informs the reason of the drone's behaviour. If this level of intention can be estimated, it

will be easier to predict the long-term behaviour of drones, which will ultimately help improve the performance of C-UAS systems. To the best of our knowledge, drones' mission estimation methods fully based on radar's kinematic measurements have yet to be reported in the open scientific literature.

The rest of the paper is organised as follows. The detailed method for data-driven setting of the ADIB is explained in Section 2. Subsequently, Section 3 explains the method to determine the intention of a drone using the naive Bayes classifier. The performance of the proposed algorithm is demonstrated in Section 4. Section 5 summarises and concludes this paper.

2 | ASSET-DEPENDENT INTENTION BANK

The possible set of malicious intents can vary depending on the characteristics of each asset. For example, smuggling by drones is likely to occur near prisons and is an intentional act. Obstruction to manned aircraft during take-off or landing is likely to occur near airports and may be intentional or accidental. Considering this range of possibilities, we can conclude that it is reasonable to compose a different set of intention candidates for each asset and utilise this set to infer the drones' intent. The set of intention candidates and its characteristics used by the proposed intention estimation algorithm is referred to as *ADIB (Asset-Dependent Intention Bank)*. The following sub-sections describe the definition of intention-specific features and a technique for establishing the ADIB, with the overall work process depicted in Figure 2a.

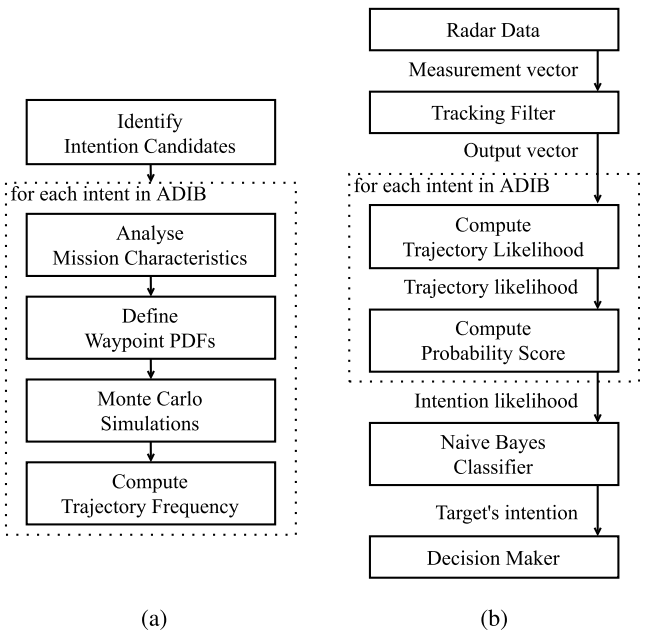

FIGURE 2 (a) Work process for establishing the ADIB, (b) Processing chain of intention estimation using ADIB.

2.1 | Behaviour analysis for each intention

First, we analyse the mission characteristics for image acquisition, smuggling, and kamikaze attacks, which are general categories of representative missions that hostile drones can perform and infer the behavioural characteristics of drones based on this analysis.

2.1.1 | Image acquisition

Suppose a drone's mission is to capture images of an asset's specific target or area. The performance of the drone's built-in camera limits the maximum allowable range between the drone and the asset during the image-recording activity. This is because the drone has to secure the minimum pixel size of its target on the captured image, which is required by the mission. During the image-recording activity, the speed and angular rate of the drone are also restricted to some extent to prevent blurry images from being captured. If the drone's target is partly surrounded by buildings or structures, the permissible approaching direction of the drone can be also restricted in order to exclude occluding obstacles on the captured images.

2.1.2 | Smuggling

Suppose a drone's mission is to deliver smuggled items to its receiver. The drone flies to a specific point where smuggling is most likely to occur. After reaching a pre-planned point within the asset, the drone may land waiting for pick-up of the smuggled items, or drop them and then return to its base. In both cases, the drones must enter a specific area near or at the asset, and keep sufficiently low speed and altitude to avoid damaging the smuggled items during delivery.

2.1.3 | Kamikaze attack

Suppose a drone's mission is to hit a target located at the asset to cause maximum physical damage via a kamikaze attack. The kamikaze attack can be committed using drone swarms to maximise the survivability against C-UAS systems attempting to neutralise them. The drones can also store explosives to maximise their lethality. High speed is vital for drones with kamikaze attack intention, as this increases their kinetic energy, leading to higher lethality. Moreover, high speed also increases the drones' survivability because the kill probability of most C-UAS system's interdiction methods decreases when the speed of drones increases.

2.2 | Heuristic selection of measurement manifold

After identifying a bank of possible malicious intentions for a specific asset, the next step is to define the features specific to

each of them. One can expect that the evolution of the state variables shown by a drone, such as its position and velocity, will vary depending on its mission. If we can collect a large number of trajectories for a given single intention, the statistics of the trajectory dataset can be considered intention-specific features. In this study, 'state variables' refer to values derived from the radar's kinematic measurements, such as the position, velocity, and its rate of change. The word 'trajectory' refers to the series of values for each state variable stored in chronological order.

We can infer from Section 2.1 that the behavioural characteristics of each mission can be defined through relative distance, relative direction, and drone speed, which are relative geometric information between assets and drones. If we define an arbitrary multidimensional manifold composed of measurable state variables, we can use the manifolds as a space where a histogram of independent trajectory can be computed. If the trajectories used in calculating the histogram are various trajectories of drones with the same intention, the calculated histogram can be considered a statistical characteristic for the drone's intention. More specifically, the measurement space for the histogram has to satisfy the following two requirements.

- The state variables in the space must be observable using radar measurements.
- Trajectory characteristics for different intentions should be clearly demonstrated.

As in Section 2.1, drone's missions have the following characteristics in common:

(i) After reaching a certain range from the asset, perform the main mission.
(ii) There are likely to be specific directions to approach the asset from.
(iii) In the process of approaching the asset, the velocity vector is controlled in a specific direction and size.

Since the relative range between a drone and an asset is included as a parameter in all of the characteristics listed above, relative range can be a key state variable that constitutes the space for histogram computation. From the characteristic (ii) above, the direction of the line of sight vector, such as elevation and azimuth angle, between a drone and an asset also can be a state variable. Both angles can in principle be adopted as state variables that constitute the histogram calculation space, but only the elevation angle is adopted for the effective delivery of the proposed method and its performance demonstration in this work. Characteristic (iii) implies that velocity information should also be included for the histogram calculation space. Therefore, the radial velocity (rate of change of relative range) and rate of climb (vertical speed of a drone) are also selected as the state variables for the histogram calculation space. Summarising, the state variables to constitute the histogram calculation space are rearranged and defined as follows:

- ***Range***: R_{ast} denoting the drone's distance from the asset.
- ***Elevation angle***: E_{ast} denoting the drone's elevation angle from the asset. The sign convention of E_{ast} is depicted in Figure 3.
- ***Radial velocity***: $V_{r,\text{ast}}$ denoting the drone's radial velocity with respect to the asset, where a positive value means that the drone is approaching the asset.
- ***Rate of climb***: V_v denoting the vertical component of the drone's velocity vector, where the positive rate of climb implies an increase in altitude.

These state variables are now used to define the phase plane on which the histogram will be computed using the trajectory dataset.

2.2.1 | Phase plane

The phase plane is a two-dimensional space composed of two state variables. The proposed method uses three kinds of phase planes: range-elevation, range-radial velocity, and range-rate of climb phase plane, indicated by $\mathbb{P}_{RE}$, $\mathbb{P}_{RV_r}$, and $\mathbb{P}_{RV_v}$, respectively. For simplicity, $\mathbb{P}_{RX}$ will be used to refer to an arbitrary phase plane.

2.2.2 | Phase trajectory

The phase trajectory is the finite sequence of two-dimensional coordinates of the trajectory data corresponding to each phase plane. $\mathbf{T}^{\mathbb{P}_{RE}}$, $\mathbf{T}^{\mathbb{P}_{RV_r}}$, and $\mathbf{T}^{\mathbb{P}_{RV_v}}$ denote the phase trajectory in the range-elevation, range-radial velocity, and range-rate of climb phase plane, respectively. Using the trajectory dataset, each phase trajectory of a single data can be expressed as:

$$\begin{aligned}\mathbf{T}^{\mathbb{P}_{RE}} &= \left(\mathbf{x}^{\mathbb{P}_{RE}}(\tau_1), \mathbf{x}^{\mathbb{P}_{RE}}(\tau_2), \ldots, \mathbf{x}^{\mathbb{P}_{RE}}(\tau_n)\right)\\ \mathbf{T}^{\mathbb{P}_{RV_r}} &= \left(\mathbf{x}^{\mathbb{P}_{RV_r}}(\tau_1), \mathbf{x}^{\mathbb{P}_{RV_r}}(\tau_2), \ldots, \mathbf{x}^{\mathbb{P}_{RV_r}}(\tau_n)\right)\\ \mathbf{T}^{\mathbb{P}_{RV_v}} &= \left(\mathbf{x}^{\mathbb{P}_{RV_v}}(\tau_1), \mathbf{x}^{\mathbb{P}_{RV_v}}(\tau_2), \ldots, \mathbf{x}^{\mathbb{P}_{RV_v}}(\tau_n)\right),\end{aligned} \tag{1}$$

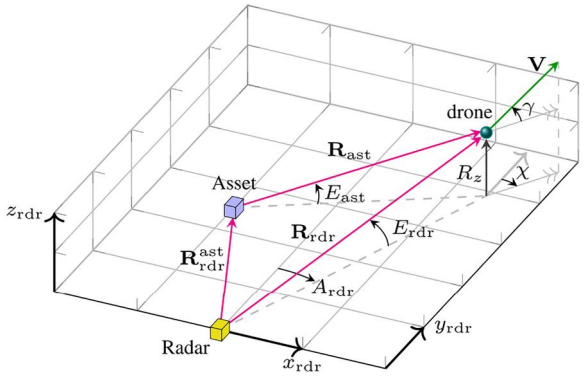

FIGURE 3 Geometry of the proposed radar simulations, with key state variables estimated by the detection and tracking processes.

where

$$\mathbf{x}^{\mathbb{P}_{RE}}(\tau_i) = \langle R_{\text{ast}}(\tau_i), E_{\text{ast}}(\tau_i)\rangle$$
$$\mathbf{x}^{\mathbb{P}_{RV_r}}(\tau_i) = \langle R_{\text{ast}}(\tau_i), V_{r,\text{ast}}(\tau_i)\rangle$$
$$\mathbf{x}^{\mathbb{P}_{RV_v}}(\tau_i) = \langle R_{\text{ast}}(\tau_i), V_v(\tau_i)\rangle.$$

τ_i is the ith time step of each dataset, and n is the total number of time steps used. $\langle\cdot\rangle$ denotes one coordinate. If N is the number of datasets used, then we can get a set of phase paths, that is

$$\begin{aligned}&\{\mathbf{T}^{\mathbb{P}_{RE}}(1), \mathbf{T}^{\mathbb{P}_{RE}}(2), \ldots, \mathbf{T}^{\mathbb{P}_{RE}}(N),\\ &\mathbf{T}^{\mathbb{P}_{RV_r}}(1), \mathbf{T}^{\mathbb{P}_{RV_r}}(2), \ldots, \mathbf{T}^{\mathbb{P}_{RV_r}}(N),\\ &\mathbf{T}^{\mathbb{P}_{RV_v}}(1), \mathbf{T}^{\mathbb{P}_{RV_v}}(2), \ldots, \mathbf{T}^{\mathbb{P}_{RV_v}}(N)\},\end{aligned} \tag{2}$$

where $\mathbf{T}^{\mathbb{P}_{RE}}(j)$, $\mathbf{T}^{\mathbb{P}_{RV_r}}(j)$, and $\mathbf{T}^{\mathbb{P}_{RV_v}}(j)$ are the phase trajectories of the jth dataset.

2.3 | Trajectory frequency on selected phase planes

The histogram of trajectories defined as in Equation (1) on the specific phase plane $\mathbb{P}_{RX}$ is called the *trajectory frequency*. To the best of our knowledge, the concept of trajectory frequency can only be found in the field of meteorology [14]. For example, Ref. [14] used the trajectory frequency for analysing statistical characteristics of an air parcel. The trajectory frequency of the air parcel provides statistics for studying climate within a specific region. Similarly, the trajectory frequency of a drone represents patterns of the drone's relative geometry to an asset.

2.3.1 | Trajectory frequency

The trajectory frequency, F, is the count of different phase trajectories in a dataset that cross over a specific region/bin on a specific phase plane. Then, the trajectory frequency matrix (TFM), $\mathbf{F}$, is the two-dimensional histogram with trajectory frequencies as the values of the histogram's bins. The trajectory frequency matrix $\mathbf{F}^{\mathbb{P}_{RX}}$ for a phase plane $\mathbb{P}_{RX}$ is defined by

$$\mathbf{F}^{\mathbb{P}_{RX}} = \begin{bmatrix} F_{11}^{\mathbb{P}_{RX}} & F_{12}^{\mathbb{P}_{RX}} & \cdots & F_{1\beta}^{\mathbb{P}_{RX}} \\ F_{21}^{\mathbb{P}_{RX}} & F_{22}^{\mathbb{P}_{RX}} & \cdots & F_{2\beta}^{\mathbb{P}_{RX}} \\ \cdots & \cdots & \cdots & \cdots \\ F_{\alpha 1}^{\mathbb{P}_{RX}} & F_{\alpha 2}^{\mathbb{P}_{RX}} & \cdots & F_{\alpha\beta}^{\mathbb{P}_{RX}} \end{bmatrix}. \tag{3}$$

The subscripts α and β indicate the number of bins for the range and the other state variable X, respectively. X may indicate elevation, radial velocity, or rate of climb. Each elements in $\mathbf{F}^{\mathbb{P}_{RX}}$ is set as

$$F_{ab}^{\mathbb{P}_{RX}} = \sum_{j=1}^{N} \mathbb{1}_{ab}\left(\mathbf{T}^{\mathbb{P}_{RX}}(j)\right), \tag{4}$$

where a and b are the row and column index of the $\mathbf{F}^{\mathbb{P}_{RX}}$. In (4), $\mathbb{1}_{ab}\left(\mathbf{T}^{\mathbb{P}_{RX}}(j)\right)$ is the indicator function defined by

$$\mathbb{1}_{ab}\left(\mathbf{T}^{\mathbb{P}_{RX}}(j)\right) \tag{5}$$
$$\stackrel{\text{def}}{=} \begin{cases} 1 & \text{if there exists } \langle R_{\text{ast}}, X\rangle \in \mathbf{T}^{\mathbb{P}_{RX}}(j), \\ & \text{where } R_{\text{ast}} \in [lb_a, ub_a) \text{ and } X \in [lb_b, ub_b). \\ 0 & \text{otherwise,} \end{cases}$$

where lb_a, ub_a, lb_b, and ub_b denote the lower bound (lb) and the upper bound (ub) of the ath range bin and bth X's bin. Figure 4 illustrates how the trajectory frequency can be computed for the range-radial velocity phase plane as an example.

After performing computation of trajectory frequency for each intention, nine different trajectory frequency datasets are generated (three intentions times three phase planes) which are

$$\begin{aligned}&\{\mathbf{F}_I^{\mathbb{P}_{RE}}, \mathbf{F}_I^{\mathbb{P}_{RV_r}}, \mathbf{F}_I^{\mathbb{P}_{RV_v}},\\ &\mathbf{F}_S^{\mathbb{P}_{RE}}, \mathbf{F}_S^{\mathbb{P}_{RV_r}}, \mathbf{F}_S^{\mathbb{P}_{RV_v}},\\ &\mathbf{F}_K^{\mathbb{P}_{RE}}, \mathbf{F}_K^{\mathbb{P}_{RV_r}}, \mathbf{F}_K^{\mathbb{P}_{RV_v}}\},\end{aligned} \tag{6}$$

where the subscripts I, S, and K denote image acquisition, smuggling, and kamikaze attack intention, respectively. In the rest of this paper, the subscript $\mathbb{I}$ will be used to refer to an arbitrary intention. The trajectory frequency datasets include the statistical characteristics of each intention and are utilised for computing the intention likelihood defined in Section 3.

2.4 | Numerical simulation-based trajectory generation

Ideally, it would be preferable to use actual experimental data for establishing the ADIB. However, this would be challenging

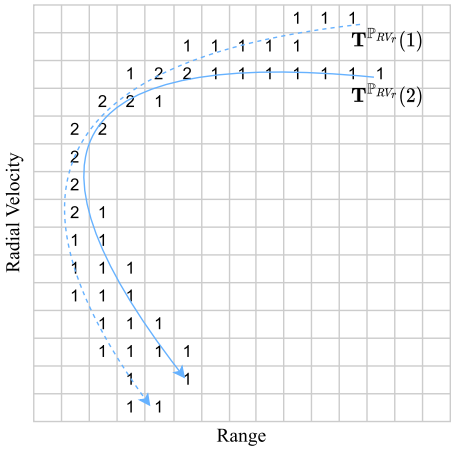

FIGURE 4 Trajectory frequency of two phase trajectories: $\mathbf{T}^{\mathbb{P}_{RV_r}}(1)$ and $\mathbf{T}^{\mathbb{P}_{RV_r}}(2)$. The number of each bin indicates the total number of phase trajectories that visited the bin. Empty bins indicate the bin with zero crossing trajectories.

and requiring to perform thousands of flights to obtain such a large dataset. As an alternative, this paper proposes a Monte Carlo simulation-based trajectory pattern generation method.

2.4.1 | Waypoint-following behaviour model

We adopt the *waypoint-following behaviour model* [15] to generate a large amount of data with intention-specific trajectories. In this model, all intentional behaviours of drones are mimicked by simple waypoint-following flights, whereby the position and speed constraints of each waypoint govern the drones' motion. This behaviour modelling method is chosen to provide a rapid and efficient trajectory simulation technique with low computational burden. Effects such as wind and related oscillations of the drones and uncertainties in their motion are not modelled for now but can be added in future versions of the simulations. It should be noted that the waypoints are used here to mimic mission-dependent trajectory patterns, and they do not necessarily coincide with waypoints set for the automatic flight control system of the drones.

2.4.2 | Waypoints generation

For a systematic setting of waypoints, it is assumed that they only exist within three regions in the surveillance area: *inbound area*, *mission area*, and *outbound area*. The number of waypoints in each area can be restricted to a specific number whenever necessary. Each area is defined as follows:

- ***Inbound Area***: The inbound area indicates a specific region in the surveillance area where the surveillance system is likely to detect a drone's first signature. The inbound area can vary depending on the conditions of the asset and the surrounding environment. Drones can pop up anywhere in the surveillance area if the asset is located in the centre of an urban area where many vehicles and humans always exist. On the contrary, if the asset is isolated in an area where civilian access is prohibited, drones will be first detected near the boundary of the surveillance area.
- ***Mission area***: The mission area indicates a specific region in the surveillance area where a drone performs the main activity of the mission. Recording images, releasing smuggled items, and hitting a target are expected to occur in the mission area of the image acquisition, smuggling, and kamikaze attack intention, respectively.
- ***Outbound Area***: The outbound area indicates a specific region in the surveillance area where the surveillance system is likely to lose a retreating drone's track. Like the inbound area, the outbound area can vary depending on the conditions of the asset and the surrounding environment. Meanwhile, some missions do not have an outbound area since they do not include a 'return' phase, such as smuggling by delivering both drone and forbidden items and kamikaze attacks.

In order to generate random waypoints in a Monte Carlo fashion, each area must provide its waypoints' probability density functions (PDFs) of position and speed values for the drones' flying trajectories. A rigorous definition of such PDFs would require quantification of factors such as drones' flight performance, camera (or other payloads) mass, navigation/guidance accuracy, random movements of drones and targets, wind/gust strength, drone surveillance system's tracking accuracy, amongst others. In this study, the PDFs for each waypoint area are instead defined based on simpler assumptions, which will be explained later in Section 4. These are still valid to demonstrate the performance of the proposed algorithm and can be made more complex and realistic in further iterations beyond the scope of this paper.

The waypoints within the mission area and outbound area have position and speed constraints, but the very first waypoint within the inbound area has additional uncertainties in two direction angles: flight path angle γ and course angle χ, which are defined in Figure 3. These direction angles are also randomly set, drawing their values from a uniform distribution between a given minimum and maximum.

2.4.3 | Simulation framework

The simulation framework used for the Monte Carlo simulation is the *RAPID-SIM*, which the authors have developed to model the radar signatures of small UAVs [16]. The *RAPID-SIM* consists of radar, drone, environment, and simulation control modules as depicted in Figure 5. For establishing an intention-specific dataset consisting of the diverse trajectories of the aforementioned state variables, Monte Carlo simulations are performed for each intention. For each run of the Monte Carlo simulations, the different sets of waypoints are generated using the waypoint uncertainty models mentioned in Section 2.4.2. The following assumptions and settings are applied for generating intention-specific trajectories:

- Consider the drone as a point mass since the accurate simulation of rotational motion is not necessary.
- The lateral acceleration control loop and the speed control loop are modelled as first-order lag systems.
- Proportional Navigation Guidance (PNG) law is applied to generate lateral acceleration to follow the current waypoint [17].
- Target waypoint is switched to the next waypoint if the drone approached the current waypoint close enough [15].

3 | INTENTION ESTIMATION USING ADIB

The following sub-sections describe the proposed method to determine the intention of a drone using radar data and the established ADIB dataset. First, the conventional signal

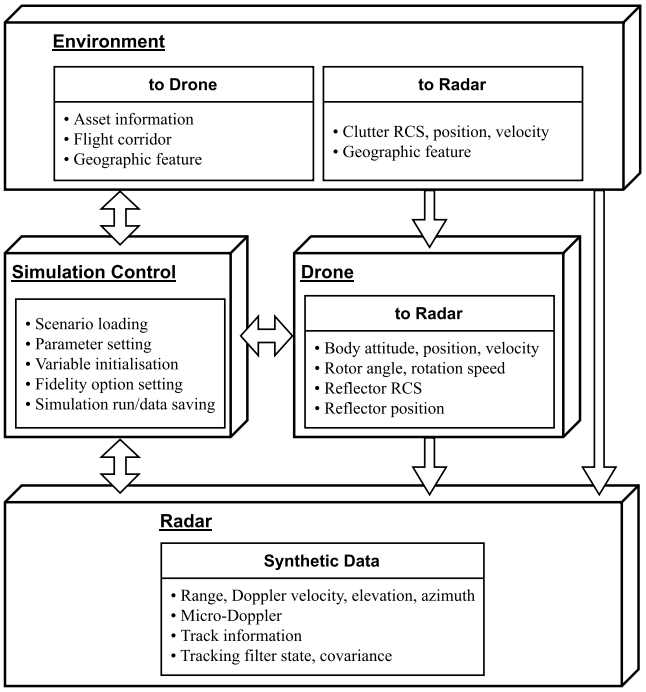

FIGURE 5 Message and data interface between modules of *RAPID-SIM*. The simulation control module sets every other modules' parameters and the initial value of variables based on users' scenario setting. The environment module provides asset and flight corridor information that may affect a drone's behaviour. The drone module computes the position and velocity of each electromagnetic scatter point that is essential for the radar module to generate synthetic radar data. The radar module generates range-Doppler data, micro-Doppler signatures, and tracking filter-based information such as state variables and their covariance.

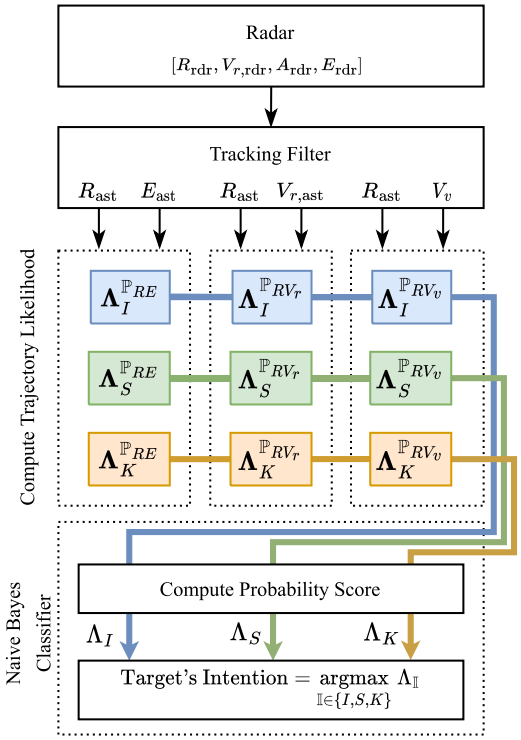

FIGURE 6 Process chain of intention estimation using trajectory likelihood and the naive Bayes classifier.

processing flow for FMCW radar is briefly provided in Section 3.1. Section 3.2 justifies the introduction of the naive Bayes classifier for the estimation of intentions and introduces the concept of *trajectory likelihood*, which is computed using the trajectory frequency. Finally, Section 3.3 explains the decision algorithm based on the naive Bayes classifier and its application to the intention inference problem. Figure 6 illustrates the proposed process chain to determine the drone's intention.

3.1 | Primary measurements of staring FMCW radar

The data recorded by the multiple channels of the FMCW radar are organised in a digitised radar cube. Its three dimensions indicate the number of receive channels, the fast-time (i.e., digitised samples for each radar chirp) and the slow-time (i.e., individual chirps received one after the other). By applying a double FFT in the fast and slow time directions, range-Doppler maps can be generated [18], that is, 2D matrices from which the range and the radial velocity of the targets can be estimated. This is done by first running detection algorithms such as CA-CFAR (Cell-Averaging Constant False Alarm Rate) on the range-Doppler maps in order to detect the cells (pixels) containing targets and reject noise and clutter. From these detected cells with targets' signature, the range R_{rdr} and radial velocity $V_{r,\text{rdr}}$ are estimated [19]. The direction of arrival (DoA) then indicates the angular orientation of a target to the radar [20, 21]. Using the 2D planar-array antenna, the azimuth A_{rdr} and elevation E_{rdr} angles of each target can be estimated, with these angles depicted in Figure 3. Hence, the measurement vector of the radar, $\mathbf{z}$, can be defined as

$$\mathbf{z} = [R_{\text{rdr}} \quad V_{r,\text{rdr}} \quad A_{\text{rdr}} \quad E_{\text{rdr}}]^{\intercal}. \tag{7}$$

The tracking filter reduces the noise within the measurements and estimates the necessary variables that are not directly measured by the CFAR detection and DoA estimation, such as the four state variables, R_{ast}, E_{ast}, $V_{r,\text{ast}}$, and V_v, defined in Section 2.4.3. To avoid confusion, the state variables forming the ADIB are assumed to be outputs of the tracking filter. Thus, the output vector, $\mathbf{y}$, is

$$\mathbf{y} = [R_{\text{ast}} \quad E_{\text{ast}} \quad V_{r,\text{ast}} \quad V_v]^{\intercal}. \tag{8}$$

Details of the tracking filter equations are explained in the Appendix.

3.2 | Trajectory likelihood matrix

The trajectory frequency matrix (TFM) shown in Equation (6) describes how frequently an arbitrary coordinate is presented on a specific phase plane for each intention. This feature can

be used as a look-up table (LUT) to calculate metrics of trajectory likelihood. For example, if the state variable of a drone at a particular time falls within an area with a high trajectory frequency of a particular TFM, $\mathbf{\Lambda}_{\mathbb{I}}^{\mathbb{P}_{RX}}$, the drone is considered to have high trajectory similarity to the intention $\mathbb{I}$ with respect to the phase plane $\mathbb{P}_{RX}$. On the contrary, if the state variable exists within a specific TFM where the trajectory frequency is zero, the drone can be considered to have low trajectory similarity with the intention $\mathbb{I}$ with respect to the phase plane $\mathbb{P}_{RX}$.

In order to use the TFM as a metric of similarity, we need to convert it to a probabilistic model. For the phase plane $\mathbb{P}_{RX}$, the probabilistic model should provide the probability:

$$P\left(\mathcal{Z}^{\mathbb{P}_{RX}}|\mathcal{C}_{\mathbb{I}}\right), \tag{9}$$

where the observed coordinate $\mathcal{Z}^{\mathbb{P}_{RX}}$ is an element of the set $\boldsymbol{\mathcal{Z}} = \left\{\mathcal{Z}^{\mathbb{P}_{RE}}, \mathcal{Z}^{\mathbb{P}_{RV_r}}, \mathcal{Z}^{\mathbb{P}_{RV_v}}\right\}$ and $\mathcal{Z}^{\mathbb{P}_{RX}} = \langle \hat{R}_{\text{ast}}, \hat{X}\rangle$. $\mathcal{C}_{\mathbb{I}}$ is an element of the intention classification set $\boldsymbol{\mathcal{C}} = \{\mathcal{C}_I, \mathcal{C}_S, \mathcal{C}_K\}$. Finding a function that provides a probability over the entire range of the observation vector is equivalent to finding a probability density function that provides the probability of a particular observation $\boldsymbol{\mathcal{Z}}$ given the true intention $\mathcal{C}_{\mathbb{I}}$.

Trajectory likelihood matrix (TLM) is an empirical estimation of the PDF that corresponds to Equation (9). In the event space we are dealing with, a single event is an increment of each element of the TFM by one. The total number of events is therefore the sum of all the elements of the TFM. Since probability can be expressed as the ratio of the number of specific events to the total number of events, we can define the TLM as follows.

Let the TLM $\mathbf{\Lambda}_{\mathbb{I}}^{\mathbb{P}_{RX}}$ be the PDF for the phase plane $\mathbb{P}_{RX}$. Then, the trajectory likelihood matrix is defined by

$$\mathbf{\Lambda}_{\mathbb{I}}^{\mathbb{P}_{RX}} = \begin{bmatrix} \Lambda_{11}^{\mathbb{P}_{RX}} & \Lambda_{12}^{\mathbb{P}_{RX}} & \cdots & \Lambda_{1\beta}^{\mathbb{P}_{RX}} \\ \Lambda_{21}^{\mathbb{P}_{RX}} & \Lambda_{22}^{\mathbb{P}_{RX}} & \cdots & \Lambda_{2\beta}^{\mathbb{P}_{RX}} \\ \cdots & \cdots & \cdots & \cdots \\ \Lambda_{\alpha 1}^{\mathbb{P}_{RX}} & \Lambda_{\alpha 2}^{\mathbb{P}_{RX}} & \cdots & \Lambda_{\alpha\beta}^{\mathbb{P}_{RX}} \end{bmatrix}, \tag{10}$$

where

$$\Lambda_{ab}^{\mathbb{P}_{RX}} = \frac{F_{ab}^{\mathbb{P}_{RX}}}{\sum_{i,j} F_{ij}^{\mathbb{P}_{RX}}}. \tag{11}$$

Since the TLM (10) is a finite 2D table, a 2D interpolation method is necessary to evaluate the trajectory likelihood of arbitrary phase coordinates consisting of real numbers. Let $\hat{\Lambda}_{\mathbb{I}}^{\mathbb{P}_{RX}}(t_k)$ be the interpolated trajectory likelihood at the tracking filter's update time step t_k. That is

$$\hat{\Lambda}_{\mathbb{I}}^{\mathbb{P}_{RX}}(t_k) = \text{BLI}\left(\mathbf{\Lambda}_{\mathbb{I}}^{\mathbb{P}_{RX}}, \langle \hat{R}_{\text{ast}}(t_k), \hat{X}(t_k)\rangle\right), \tag{12}$$

where $\text{BLI}(\mathbf{A}, \langle x, y\rangle)$ is the Bilinear Interpolation (BLI) function with 2D grid data A, and the 2D query points, x and y [22]. We need three sets of query points which are $\langle \hat{R}_{\text{ast}}(t_k), \hat{E}_{\text{ast}}(t_k)\rangle$, $\langle \hat{R}_{\text{ast}}(t_k), \hat{V}_{r,\text{ast}}(t_k)\rangle$, and $\langle \hat{R}_{\text{ast}}(t_k), \hat{V}_v(t_k)\rangle$. All query points can be set using the output vector in Equation (28) in the Appendix. After computing all interpolated trajectory likelihoods for each intention and each phase plane at t_k, we get nine scalar values that are

$$\begin{aligned} &\Big\{\hat{\Lambda}_I^{\mathbb{P}_{RE}}(t_k), \hat{\Lambda}_I^{\mathbb{P}_{RV_r}}(t_k), \hat{\Lambda}_I^{\mathbb{P}_{RV_v}}(t_k), \\ &\hat{\Lambda}_S^{\mathbb{P}_{RE}}(t_k), \hat{\Lambda}_S^{\mathbb{P}_{RV_r}}(t_k), \hat{\Lambda}_S^{\mathbb{P}_{RV_v}}(t_k), \\ &\hat{\Lambda}_K^{\mathbb{P}_{RE}}(t_k), \hat{\Lambda}_K^{\mathbb{P}_{RV_r}}(t_k), \hat{\Lambda}_K^{\mathbb{P}_{RV_v}}(t_k)\Big\}. \end{aligned} \tag{13}$$

The subscripts indicate specific intentions, the same as in Equation (6). Now we can consider that the conditional probability in Equation (9) can be computed using Equation (12). That is,

$$P\left(\mathcal{Z}^{\mathbb{P}_{RX}}|\mathcal{C}_{\mathbb{I}}\right) = \hat{\Lambda}_{\mathbb{I}}^{\mathbb{P}_{RX}}. \tag{14}$$

3.3 | Naive bayes classifier

In Section 3.2, we defined a method that computes the individual probability $P\left(\mathcal{Z}^{\mathbb{P}_{RX}}|\mathcal{C}_{\mathbb{I}}\right)$ of each observation coordinate for a given intention. The intention estimation problem, on the other hand, requires deriving a probability model that computes the intention probability $P(\mathcal{C}_{\mathbb{I}}|\boldsymbol{\mathcal{Z}})$ from all the given observation coordinates. Using Bayes' theorem, the following expression is derived

$$P(\mathcal{C}_{\mathbb{I}}|\boldsymbol{\mathcal{Z}}) = \frac{P(\mathcal{C}_{\mathbb{I}})P(\boldsymbol{\mathcal{Z}}|\mathcal{C}_{\mathbb{I}})}{P(\boldsymbol{\mathcal{Z}})}. \tag{15}$$

Calculating the value of the denominator in the above equation is not straightforward, as the total probability of a particular set of the observation coordinate changes significantly depending on the type of behavioural or intention models considered. However, if the goal of intention estimation is to find the most likely intention that a particular target might have, the denominator of Equation (15) does not need to be found. We can use a naive Bayes classifier to solve this problem.

Applying a naive Bayes model [23], the conditional probability of the class $\mathcal{C}_{\mathbb{I}}$ given the observation coordinates $\boldsymbol{\mathcal{Z}}$ satisfies the following expression:

$$P(\mathcal{C}_{\mathbb{I}}|\boldsymbol{\mathcal{Z}}) = \frac{P(\mathcal{C}_{\mathbb{I}})\Pi_{j=1}^{3} P\left(\mathcal{Z}_j|\mathcal{C}_i\right)}{P(\boldsymbol{\mathcal{Z}})}, \tag{16}$$

where $\mathcal{Z}_1 = \mathcal{Z}^{\mathbb{P}_{RE}}$, $\mathcal{Z}_2 = \mathcal{Z}^{\mathbb{P}_{RV_r}}$, and $\mathcal{Z}_3 = \mathcal{Z}^{\mathbb{P}_{RV_v}}$. By using Equation (14), $P\left(\mathcal{Z}_j|\mathcal{C}_i\right)$ in Equation (16) corresponds to $\hat{\Lambda}_{\mathbb{I}}^{\mathbb{P}_{RX}}$ in Equation (12). Then, Equation (16) is transformed to

$$P(\mathcal{C}_{\mathbb{I}}|\boldsymbol{\mathcal{Z}}) = \frac{P(\mathcal{C}_{\mathbb{I}})\hat{\Lambda}_{\mathbb{I}}^{\mathbb{P}_{RE}}\hat{\Lambda}_{\mathbb{I}}^{\mathbb{P}_{RV_r}}\hat{\Lambda}_{\mathbb{I}}^{\mathbb{P}_{RV_v}}}{P(\boldsymbol{\mathcal{Z}})}. \quad (17)$$

Assuming that all the intention classes in Equation (17) have the same prior probability $P(\mathcal{C}_{\mathbb{I}})$ and that $P(\boldsymbol{\mathcal{Z}})$ is identical for all classes, the multiplication between the interpolated trajectory likelihoods of the equation can be defined as the probability score of $\mathcal{C}_{\mathbb{I}}$. That is

$$\Lambda_{\mathbb{I}} = \hat{\Lambda}_{\mathbb{I}}^{\mathbb{P}_{RE}}\hat{\Lambda}_{\mathbb{I}}^{\mathbb{P}_{RV_r}}\hat{\Lambda}_{\mathbb{I}}^{\mathbb{P}_{RV_v}}, \quad (18)$$

where the probability score $\Lambda_{\mathbb{I}}$ is considered as the likelihood of the intention $\mathcal{C}_{\mathbb{I}}$. Then, the class decision rule based on the likelihood of each intention in the ADIB can be set as

$$\text{Target's} \quad \text{Intention} = \underset{\mathbb{I}\in\{I,S,K\}}{\text{argmax}}\ \Lambda_{\mathbb{I}}. \quad (19)$$

As shown in the block diagram of Figure 2b, the intention likelihoods for each intention as in Equation (18) are computed independently. Therefore, the proposed algorithm has a time complexity of $O(n)$, or a linear time algorithm, where n is the number of intention candidates considered in the ADIB.

4 | NUMERICAL SIMULATIONS AND RESULTS

This section presents the proposed approach for intention estimation via the established ADIB and the naive Bayes classifier. The ADIB consists of three intentions: image acquisition, smuggling, and kamikaze attack. We first describe the random waypoint setting for each intention in Section 4.1 and review the intention estimation results in Section 4.2 (image acquisition), 4.3 (smuggling), and 4.4 (kamikaze attack). In Section 4.5, the confusion matrix generated by Monte Carlo simulations is shown, and the performance of the proposed method is analysed based on it.

4.1 | Definition of the ADIB

To compute the trajectory likelihood matrix (10) for each intention and each phase plane, we need to define the PDFs for the waypoints of each intention, assuming that a virtual mission analysis for feasible intentions was performed. The analysis results can be found in Tables 1–3, where each table shows the values used for defining the PDFs at each waypoint for image acquisition, smuggling, and kamikaze attack mission, respectively. In the tables, U (a, b) denotes the uniform distribution with the lower bound, a, and the upper bound, b. For the inbound area, the initial waypoint's position, speed, and direction are randomly set, while for the mission and outbound area, only the position and required speed of the waypoints are randomly set. As mentioned in Section 2.4.2, systematic errors such as winds and navigation errors were not considered. However, the noise for the radar measurements was applied in a realistic manner.

Figure 7 shows the changes of the trajectory likelihood matrix, $\boldsymbol{\Lambda}_I^{\mathbb{P}_{RV_r}}$, as the number of the total Monte Carlo run, N, increases. The figure shows that the trajectory likelihood matrix converges to a specific shape as N increases, hence a sufficiently large N is needed to secure reliable results for intention estimation. Using the PDFs defined in Tables 1–3, Monte Carlo simulations were performed with $N = 1000$ for each mission. The computed trajectory likelihood matrices (10) are illustrated later in this section in Figures 9, 12, and 15, with arbitrary phase trajectories corresponding to each scenario.

It is important to note that in Figures 9, 12, and 15, the areas with the same colour in different phase planes do not necessarily represent the same likelihood, as the colours only indicate the relative difference in likelihood within the same

TABLE 1 Image acquisition's PDFs for waypoints definition.

Variable	Inbound area WP1	Mission area WP2	Mission area WP3	Outbound area WP4
$R_{x,\text{rdr}}$ [m]	U (−300,300)	U (−100,0)	U (−100,0)	U (−300,300)
$R_{y,\text{rdr}}$ [m]	U (400,500)	U (150,250)	U (150,250)	U (400,500)
$R_{z,\text{rdr}}$ [m]	U (20,100)	U (20,50)	U (20,50)	U (20,100)
V [m/s]	U (23,27)	U (23,27)	U (1,3)	U (23,27)
χ [deg]	U (178,182)	-	-	-
γ [deg]	U (3,7)	-	-	-

TABLE 2 Smuggling's PDFs for waypoints definition.

Variable	Inbound area WP1	Mission area WP2	Mission area WP3	Outbound area WP4
$R_{x,\text{rdr}}$ [m]	U (−300,300)	U (50,150)	U (80,120)	U (−300,300)
$R_{y,\text{rdr}}$ [m]	U (400,500)	U (250,300)	U (180,220)	U (400,500)
$R_{z,\text{rdr}}$ [m]	U (20,100)	U (10,20)	U (10,20)	U (20,100)
V [m/s]	U (23,27)	U (23,27)	U (1,5)	U (23,27)
χ [deg]	U (178,182)	-	-	-
γ [deg]	U (3,7)	-	-	-

TABLE 3 Kamikaze attack's PDFs for waypoints definition.

Variable	Inbound area WP1	Mission area WP2
$R_{x,\text{rdr}}$ [m]	U (−300,300)	U (80,120)
$R_{y,\text{rdr}}$ [m]	U (400,500)	U (180,220)
$R_{z,\text{rdr}}$ [m]	U (20,100)	U (0,0)
V [m/s]	U (23,35)	-
χ [deg]	U (178,182)	-
γ [deg]	U (3,7)	-

phase plane of each intention. The colour bars for each TLM figure have been omitted not to have too many objects in these figures, but the actual TLM values can be seen separately in Figures 10, 13, and 16.

4.2 | Image acquisition scenario

Figure 8 illustrates the spatial locations for each waypoint area defined by the virtual mission analysis for the *image acquisition* mission. The mission area of the image acquisition mission is defined as the ideal area to get the best image quality of the target at the asset. Arbitrary waypoints and trajectory for the image acquisition are also illustrated in Figure 8. The first signal of the drone was detected in waypoint 1. The drone decelerated its speed after reaching waypoint 2 to secure stable

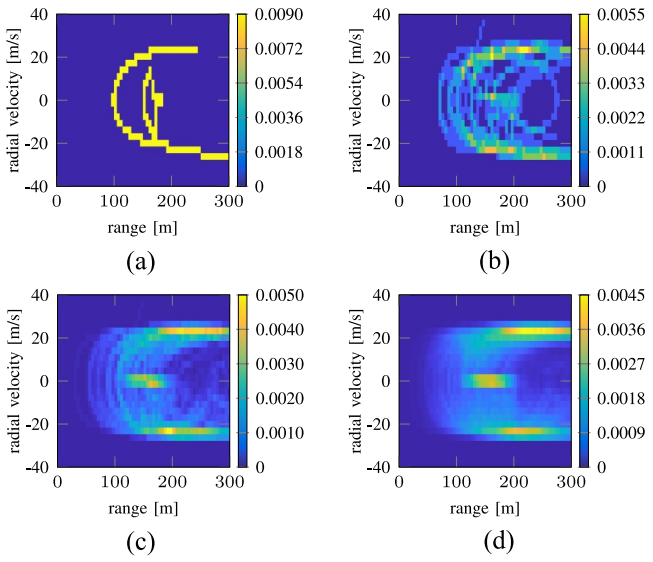

FIGURE 7 The trajectory likelihood matrix, $\mathbf{\Lambda}_I^{\mathbb{P}_{RV_r}}$, for various N, the number of Monte Carlo simulations. (a) $N = 1$, (b) $N = 10$, (c) $N = 100$, (d) $N = 1000$.

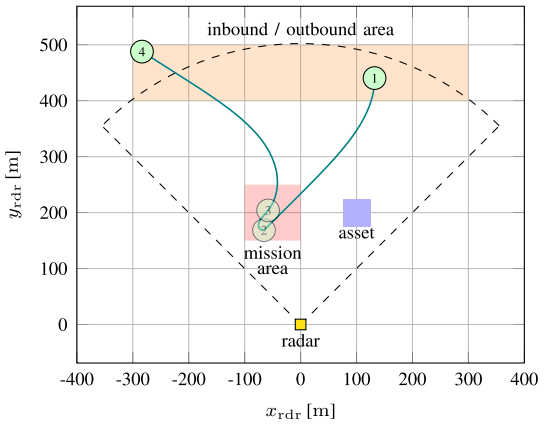

FIGURE 8 A mission area plus arbitrary waypoints and trajectory of 'image acquisition' scenario. The dashed line represents the approximate area under surveillance.

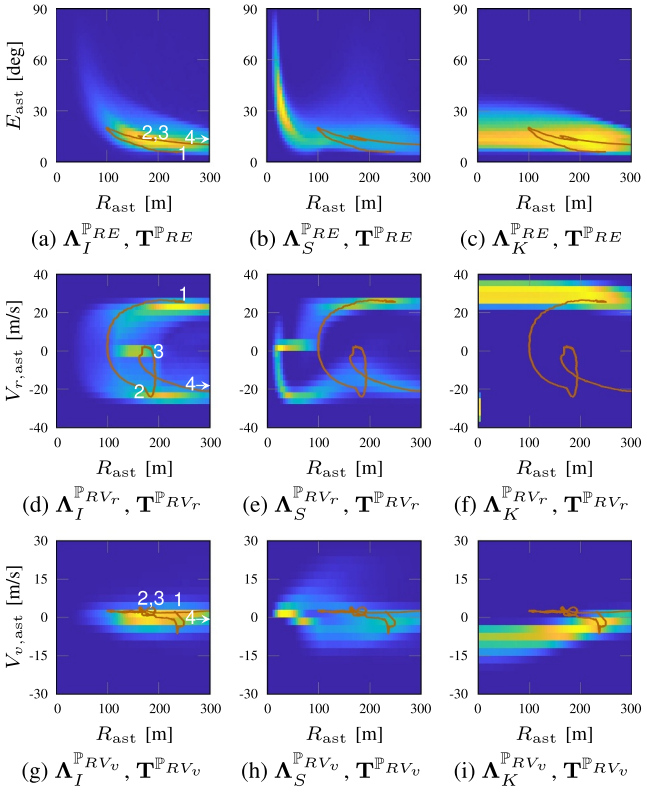

FIGURE 9 Trajectory likelihood matrices computed from 1000 Monte Carlo simulations and phase trajectories (brown lines) of image acquisition scenario corresponding to each phase plane.

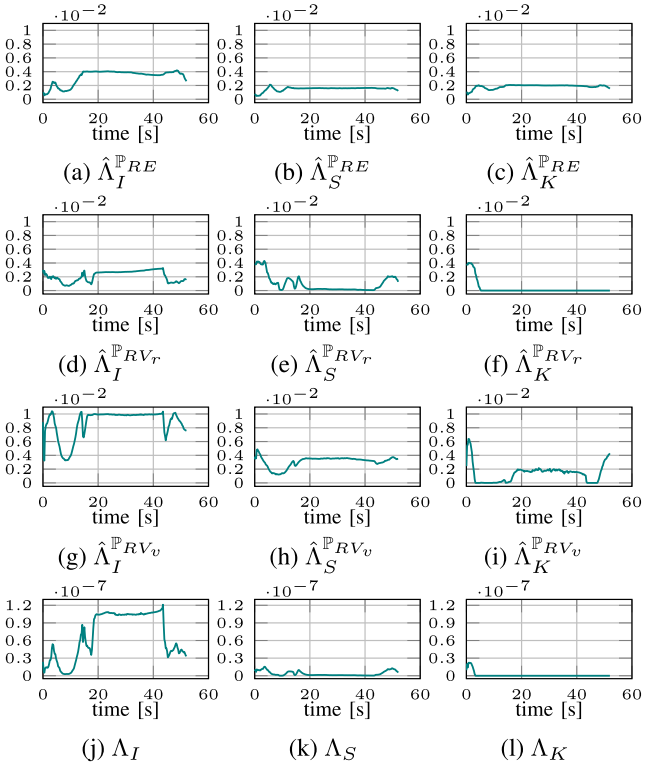

FIGURE 10 (a)-(i) Interpolated trajectory likelihood of image acquisition scenario corresponding to each phase plane. The final computed intention likelihood of image acquisition, smuggling, and kamikaze are shown in (j), (k), and (l), respectively.

image quality. The image acquisition was continued until the drone reached waypoint 3. After finishing the image acquisition, the drone escaped the surveillance area by flying to waypoint 4.

For brevity, let the high-TL (Trajectory Likelihood) region and low-TL region indicate the regions where the elements of the computed trajectory likelihood matrix are high and low, respectively. Figure 9 illustrates the trajectory likelihood matrices and the drone's phase trajectories on each phase plane, whereas Figure 10 shows the computed trajectory likelihoods and intention likelihoods of the image acquisition scenario. In each phase plane in Figure 9, the bright yellow and dark blue indicate high-TL and low-TL region within the phase plane, respectively. The white numbers are the indices of the waypoints, and the position of the waypoint on the graph indicates the approximate coordinates when the target passes through that waypoint. In Figure 9a,d,g, it is clearly observed that the phase trajectories tend to converge in high-TL region of the actual intention's (i.e., image acquisition, in this scenario) trajectory likelihood matrix, which are $\mathbf{\Lambda}_I^{\mathbb{P}_{RE}}$, $\mathbf{\Lambda}_I^{\mathbb{P}_{RV_r}}$, and $\mathbf{\Lambda}_I^{\mathbb{P}_{RV_v}}$. Such tendency led to the image acquisition's trajectory likelihoods, $\hat{\Lambda}_I^{\mathbb{P}_{RE}}$, $\hat{\Lambda}_I^{\mathbb{P}_{RV_r}}$, and $\hat{\Lambda}_I^{\mathbb{P}_{RV_v}}$, being maintained at large values between 20 and 42 s, as illustrated in Figure 10a,d,g. The large value of image acquisition's trajectory likelihood results in the large value of image acquisition's intention likelihood, as shown in Figure 10j. It should be noted that Figures 10, 13, and 16 show trajectory likelihoods and intention likelihoods only when each phase coordinate is within the specific range of the phase plane.

4.3 | Smuggling scenario

Figure 11 illustrates the spatial locations for each waypoint area for the *smuggling* mission. Mission area 1 in Figure 11 is considered to be the ideal approaching course for smuggling, while mission area 2 is the area where the contraband items should be dropped at.

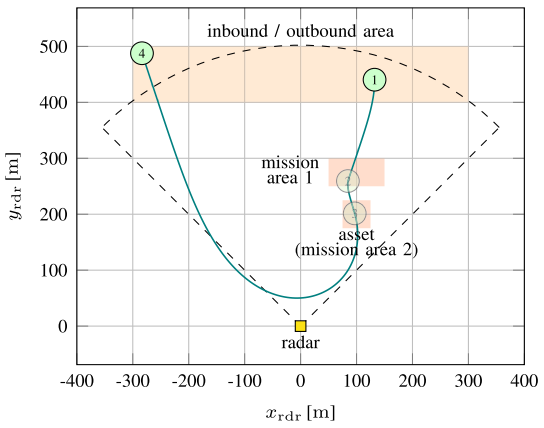

FIGURE 11 Mission areas plus arbitrary waypoints and trajectory of 'smuggling' scenario.

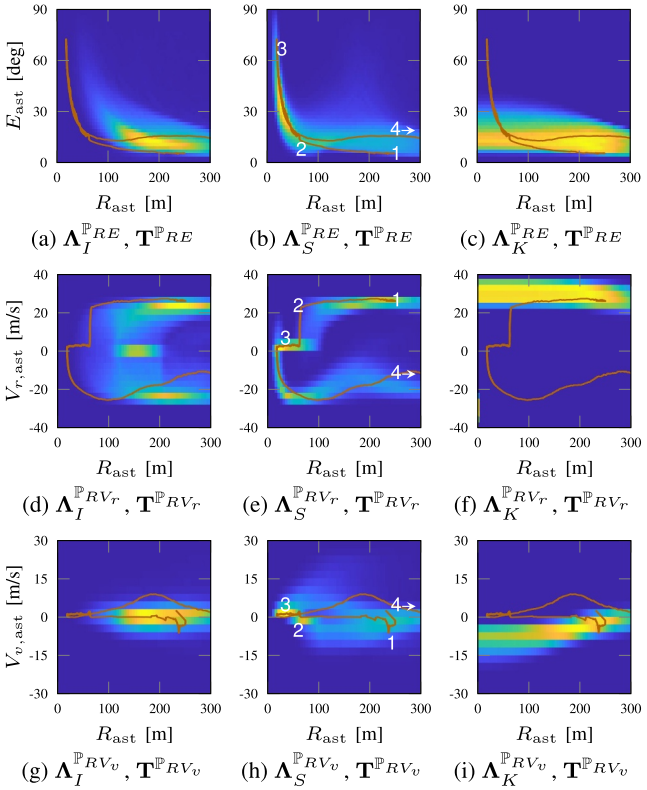

FIGURE 12 Trajectory likelihood matrices computed from 1000 Monte Carlo simulations and phase trajectories (brown lines) of smuggling scenario corresponding to each phase plane.

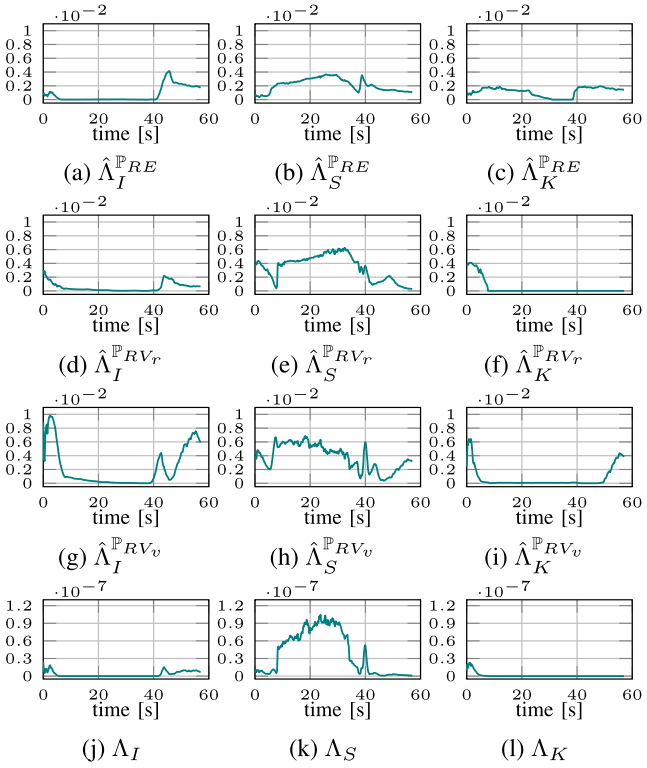

FIGURE 13 (a)-(i) Interpolated trajectory likelihood of smuggling scenario corresponding to each phase plane. The final computed intention likelihood of image acquisition, smuggling, and kamikaze are shown in (j), (k), and (l), respectively.

Arbitrary waypoints and the corresponding trajectory for smuggling are also illustrated in Figure 11. After entering the surveillance area, the drone decelerated its speed when it approached waypoint 2 to secure the safe release of contraband items. After releasing them at waypoint 3, the drone left the surveillance area.

Figure 12 illustrates the trajectory likelihood matrices and the drone's phase trajectories on each phase plane. As in the case of the image acquisition scenario, Figure 12 shows that each phase trajectory tends to converge to the high-TL region of the actual intention's trajectory likelihood matrix (i.e., the one associated with smuggling, in this scenario).

Figure 13 shows the computed trajectory likelihoods and intention likelihoods of the smuggling scenario. It is confirmed from Figure 13k that the likelihood of the actual intention, smuggling, remained high between 8 and 35 s. In contrast, other intention likelihoods of image acquisition and kamikaze attack remained low, as shown in Figure 13j,l.

Figure 12g shows that the range-rate of climb trajectory of the smuggling scenario remained in the high-TL region of the image acquisition intention's trajectory likelihood matrix at the initial phase of the scenario. The actual peak of $\hat{\Lambda}_I^{\mathbb{P}_{RV_v}}$ is 9.8×10^{-3} at $t = 2.4$ s, which can be confirmed in Figure 13g. This fact implies that it is hard to distinguish the smuggling and the image acquisition intentions using only the range-rate of climb trajectory. However, as seen in Figure 13a,d, the other trajectory likelihoods of the image acquisition intention remained low enough to prevent the final smuggling intention likelihood in Figure 13j from being high.

4.4 | Kamikaze scenario

Figure 14 illustrates the spatial locations for each waypoint area for the *kamikaze attack* mission. The mission area in Figure 14 is the same as the asset area, which is the target of the drone. Two sets of arbitrary waypoints and the trajectories for a kamikaze attack are also illustrated in Figure 14. After entering the surveillance area, the drones kept their speed until hitting the asset.

Figure 15 illustrates the trajectory likelihood matrices and the phase trajectories of two different drones with kamikaze attack intention. Let Drone-a and Drone-b denote the drones with waypoints 1-2 and 1′-2, respectively. Figure 15 shows that each phase trajectory of both drones tends to converge to the high-TL region of the actual intention's trajectory likelihood matrix (i.e., the one associated with the kamikaze attack, in this scenario). However, we can see in Figure 16 that the tendency of estimating intention for the two drones is clearly different. For Drone-a, it is confirmed from Figure 16l that the likelihood of the actual intention, kamikaze attack, remained relatively high to other intentions' likelihood during the entire scenario. On the other hand, the intention estimation result of Drone-b shows that $\Lambda_I(t) > \Lambda_K(t)$ for $8 \le t \le 11$, which can be considered as an estimation error region. The reason for this phenomenon is that the likelihood of each phase plane of kamikaze intention was slightly smaller than that of the image acquisition intention. More specifically, $\hat{\Lambda}_I^{\mathbb{P}_{RE}}(t) > \hat{\Lambda}_K^{\mathbb{P}_{RE}}(t)$ for $8 \le t \le 13.4$, $\hat{\Lambda}_I^{\mathbb{P}_{RV_r}}(t) > \hat{\Lambda}_K^{\mathbb{P}_{RV_r}}(t)$ for $8 \le t \le 10$, and $\hat{\Lambda}_I^{\mathbb{P}_{RV_v}}(t) > \hat{\Lambda}_K^{\mathbb{P}_{RV_v}}(t)$ for $8 \le t \le 10$. This phenomenon shows

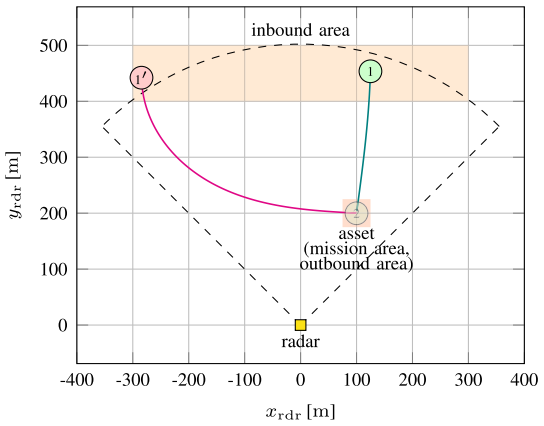

FIGURE 14 A mission area plus arbitrary waypoints and trajectories of 'kamikaze' scenario. Trajectories between waypoint 1-2 and 1′-2 are the trajectories of Drone-a and Drone-b, respectively.

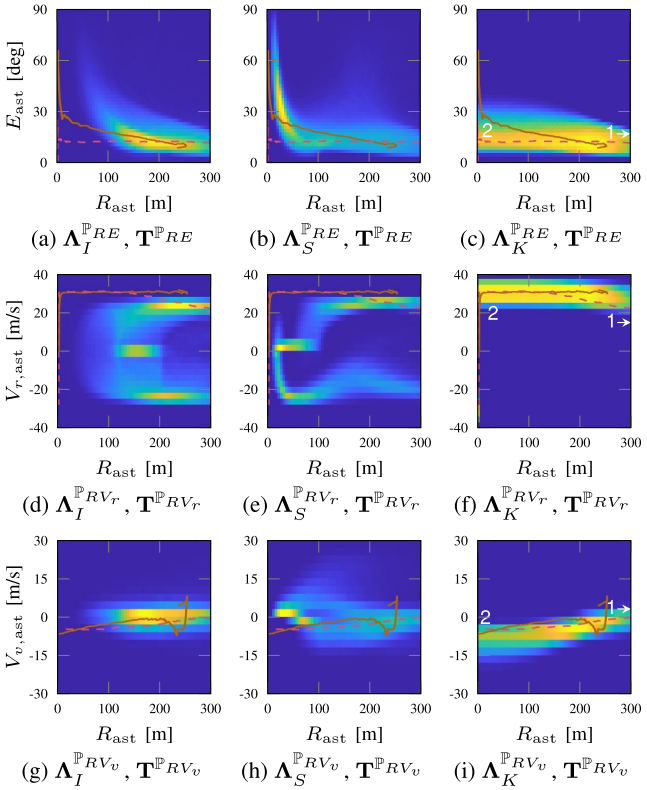

FIGURE 15 Trajectory likelihood matrices computed from 1000 Monte Carlo simulations and phase trajectories of kamikaze scenario corresponding to each phase plane. Solid lines and dashed lines are trajectories of Drone-a and Drone-b, respectively.

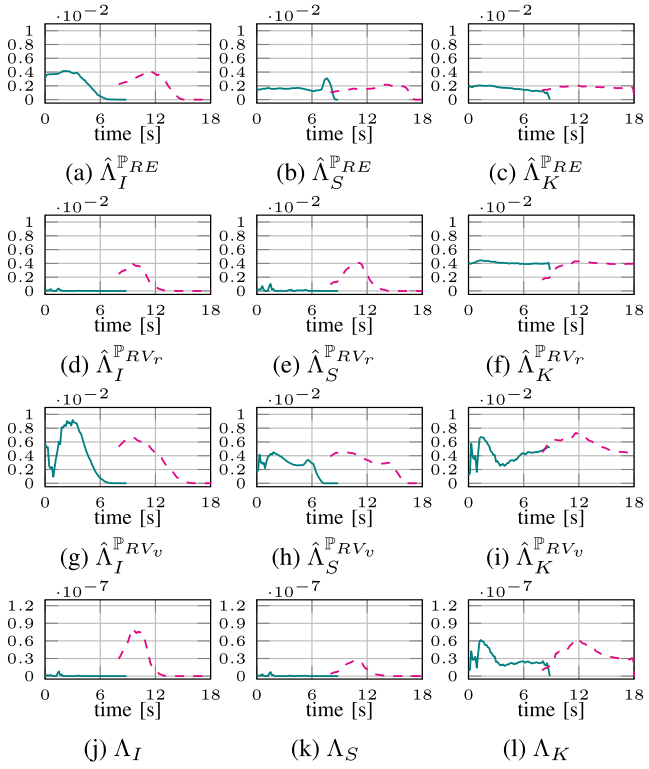

FIGURE 16 (a)-(i) Interpolated trajectory likelihood of the kamikaze scenario corresponding to each phase plane. The final computed intention likelihood of image acquisition, smuggling, and kamikaze are shown in (j), (k), and (l), respectively. Solid lines and dashed lines indicate data of Drone-a and Drone-b, respectively.

the limitation of the proposed method to estimate the intention by comparing the relative size of the probability score. In other words, it will be difficult to unambiguously choose one intention over the other for the proposed method if two intentions have similar statistical characteristics within the same region on the phase planes.

4.5 | Intention inference performance

To analyse the performance of the proposed intention estimation method, a confusion matrix was obtained using a new dataset that was not used to generate the TLMs. 100 Monte Carlo simulations for each scenario (image acquisition, smuggling, and kamikaze attack) were performed, and Figure 17 shows the computed overall confusion matrix. In the case of image acquisition, the true positive rate of accurately estimating the actual intention was the highest, but the false positive rate of estimating the intention in the case of non-image acquisition scenarios was also high. Estimating Drone-b's intention in Section 4.4 is an example of the high false positive rate in terms of estimating image acquisition, or the high false negative rate in terms of estimating kamikaze attack intention. When image acquisition was excluded, similar estimation performance for smuggling and kamikaze attack was achieved.

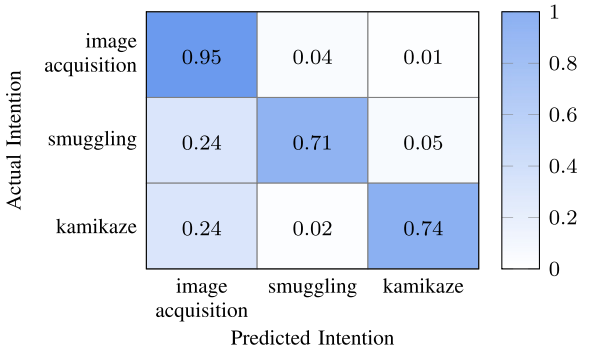

FIGURE 17 Confusion matrix computed using 100 Monte Carlo runs for each intention.

5 | CONCLUSIONS

Interest in counter-drone technology has increased dramatically in recent years. This paper proposes an autonomous intention estimation algorithm that can be applied to C-UAS or UTM (Unmanned aircraft system Traffic Management) systems. The algorithm is based on radar data, providing fast and robust intention estimation for multiple targets. The core idea of the proposed intention estimation algorithm is to build intention-specific features for each intention in advance and utilise them in actual drone surveillance situations. This intention-specific dataset is called ADIB, and it consists of statistical features of a drone's trajectory called 'trajectory frequency'. To effectively depict the characteristics of various trajectories, the trajectory frequency is computed on multiple phase planes through Monte Carlo Simulations. Using the trajectory frequency and measured radar data, we can compute the likelihood of each phase trajectory on the different phase planes. Finally, a naive Bayes classifier is applied to integrate the trajectory likelihood in different phase planes and ultimately compute the intention likelihood of all intentions concerned.

Numerical simulations for the three candidate intentions of image acquisition, smuggling, and kamikaze attack demonstrated the performance of the presented method. The simulation results show that one can estimate the true intention of a specific drone by comparing the value of each intention likelihood. However, the simulation results also showed that there is a possibility that the proposed algorithm may compute a similar degree of intention likelihood for more than one possible intention. Such a phenomenon can be caused when the two different intentions have similar trajectory frequency in their ADIB dataset, that is, similar values of the measured space variables from the radar data.

In addition, there are parts of the simulations where the intention likelihood of the actual intention drops sharply because the target passes through the low-TL (trajectory likelihood) region at that point. The longer the target stays in the low-TL region, the more the false negative rate of the intention estimation increases. This is a fundamental limitation of the current formulation of the proposed method.

Addressing these phenomena is left as future work. One possible solution is replacing the naive Bayes with a more

sophisticated yet less explainable machine learning algorithm, such as neural networks. Also, for more complicated modelling of drones' behaviour, the behaviour tree model [24] can be adopted, which may provide suitable performance in modelling interactive behaviours among different smart drones.

NOMENCLATURE

ACRONYMS

ADIB	asset-dependent intention bank
TFM	trajectory frequency matrix
TLM	trajectory likelihood matrix

SETS

$\mathcal{C}$	intention candidates
$\mathcal{Z}$	observation coordinates

INDICES

X	arbitrary state variable
$\mathbb{P}_{RX}$	phase plane of range and arbitrary state variable
$\mathbb{I}$	arbitrary intention
I	image acquisition intention
S	smuggling intention
K	kamikaze attack intention
rdr	radar
ast	asset

MATRICES

$\mathbf{T}$	phase trajectory (sequence of coordinates)
$\mathbf{F}$	trajectory frequency matrix
$\mathbf{\Lambda}$	trajectory likelihood matrix

SCALARS

A	azimuth angle
E	elevation angle
$\Lambda_{\mathbb{I}}$	intention likelihood of intention $\mathbb{I}$
$\hat{\Lambda}$	interpolated trajectory likelihood
V_r	radial velocity
R	range
V_v	rate of climb
F	trajectory frequency

VECTORS

$\mathbf{x}$	2D coordinate of specific phase plane or state vector of tracking filter
$\mathbf{z}$	measurement vector of tracking filter
$\mathbf{y}$	output vector of tracking filter

AUTHOR CONTRIBUTIONS

Joongsup Yun: Conceptualisation; Formal analysis; Investigation; Methodology; Software; Validation; Visualisation; Writing – original draft. **David Anderson**: Conceptualisation; Funding acquisition; Project administration; Resources; Supervision; Writing – review & editing. **Francesco Fioranelli**: Conceptualisation; Funding acquisition; Project administration; Resources; Supervision; Writing – review & editing.

ACKNOWLEDGEMENTS

This work relates to Department of Navy award (N62909-19-1-2073) issued by the Office of Naval Research.

CONFLICT OF INTEREST STATEMENT

None.

DATA AVAILABILITY STATEMENT

The data that support the findings of this study are available from the corresponding author upon reasonable request.

ORCID

Joongsup Yun https://orcid.org/0000-0003-2428-2498
David Anderson https://orcid.org/0000-0001-6301-9532
Francesco Fioranelli https://orcid.org/0000-0001-8254-8093

REFERENCES

1. Bilik, I., Tabrikian, J.: Chap.9 Knowledge-Based Radar Target Classification, Knowledge-Based Radar Detection, Tracking, and Classification. John Wiley & Sons, US (2008)
2. Martins, B.O., Michel, A.H., Silkoset, A.: Countering the Drone Threat. Peace Research Institute. Oslo (PRIO), 2020). https://www.prio.org/Publications/Publication/?x=12245
3. Harman, S.: A comparison of staring radars with scanning radars for UAV detection: introducing the alarm™staring radar. In: Proceedings of the 12th European Radar Conference (EuRAD). Paris (2015)
4. Patel, J., Fioranelli, F., Anderson, D.: Review of radar classification and rcs characterisation techniques for small uavs or drones. IET Radar, Sonar Navig. 12(9), 911–919 (2018). https://doi.org/10.1049/iet-rsn.2018.0020
5. Mitchell, R., Chen, I.: Adaptive intrusion detection of malicious unmanned air vehicles using behavior rule specifications. IEEE Trans. Syst. Man Cybern. Syst. 44(5), 593–604 (2014). https://doi.org/10.1109/tsmc.2013.2265083
6. Janakiraman, V., Nielsen, D.: Anomaly detection in aviation data using extreme learning machines. In: 2016 International Joint Conference on Neural Networks (IJCNN), pp. 1993–2000. Vancouver (2016)
7. Katsilieris, F., Charlish, A.: Knowledge based anomaly detection for ground moving targets. In: Proc. 2018 IEEE Radar Conference (RadarConf18), pp. 786–791. Oklahoma City (2018)
8. Azimirad, E., Haddadnia, J.: Target threat assessment using fuzzy sets theory. Int. J. Adv. Intell. Informatics 1(2), 57–74 (2015). https://doi.org/10.26555/ijain.v1i2.18
9. Liang, J., et al.: Detection of malicious intent in non-cooperative drone surveillance. In: Proceedings 2021 Sensor Signal Processing for Defence Conference (SSPD). Edinburgh (2021)
10. Wit, J., Gusland, D., Trommel, R.: Radar measurements for the assessment of features for drone characterization. In: 2020 17th European Radar Conference (EuRAD). Utrecht, Netherlands (2021)
11. Al Sa'd, M., et al.: RF-based drone detection and identification using deep learning approaches: an initiative towards a large open source drone database. Future Generat. Comput. Syst. 100, 86–97 (2019). https://doi.org/10.1016/j.future.2019.05.007
12. Wang, A., Krishnamurthy, V., Balaji, B.: Intent inference and syntactic tracking with GMTI measurements. IEEE Trans. Aero. Electron. Syst. 47(4), 2824–2843 (2011). https://doi.org/10.1109/taes.2011.6034667

13. Zhang, W., Yang, F., Liang, Y.: A Bayesian framework for joint target tracking, classification, and intent inference. IEEE Access 7, 2169–3536 (2019). https://doi.org/10.1109/access.2019.2917541
14. Rolph, G., Stein, A., Stunder, B.: Real-time Environmental Applications and Display System: READY, vol. 95, pp. 210–228. Environmental Modelling & Software (2017)
15. Beard, R., McLain, T.: In: 'Small Unmanned Aircraft: Theory and Practice, pp. 223–242. Princeton University Press, Princeton (2012)
16. Yun, J., Anderson, D., Fioranelli, F.: Parametric investigation on simulated staring FMCW radar for anti-drone swarms. In: Proceeding 2020 IEEE Radar Conference. Florence (2020)
17. Lin, C.: Guidance processing. In: Modern Navigation, Guidance, and Control Processing, pp. 359–361. Prentice–Hall, NJ (1991)
18. Barick, D.: 'FM/CW Radar Signals and Digital Processing'. (Boulder Colorado. National Oceanic and Atmospheric Administration (1973). ERL 283-WPL 26
19. Rohling, H.: Radar CFAR thresholding in clutter and multiple target situations. IEEE Trans. Aero. Electron. Syst.(4), 608–621 (1983). AES-19. https://doi.org/10.1109/taes.1983.309350
20. Schmidt, R.: Multiple emitter location and signal parameter estimation. IEEE Trans. Antenn. Propag. 34(3), 276–280 (1986). https://doi.org/10.1109/tap.1986.1143830
21. Roy, R., Kailath, T.: ESPRIT-estimation of signal parameters via rotational invariance techniques. IEEE Trans. Acoust. Speech Signal Process. 37(7), 984–995 (1989). https://doi.org/10.1109/29.32276
22. Press, W., et al.: In: 'Numerical Recipes in C: The Art of Scientific Computing, pp. 123–128. Cambridge University Press, New York (1992)
23. Rish, I.: An empirical study of the naive bayes classifier. In: IJCAI 2001 Workshop on Empirical Methods in Artificial Intelligence, pp. 41–46. Seattle, WA (2001)
24. Colledanchise, M., Ögren, P.: In: 'Behavior Trees in Robotics and AI', pp. 6–10. CRC Press, London (2019)
25. BarShalom, Y., Li, X., Kirubarajan, T.: In: 'Estimation with Applications to Tracking and Navigation: Theory, Algorithms and Software, pp. 267–275. John Wiley & Sons, NY (2001)
26. Wan, E., Merwe, R.V.D.: The unscented kalman filter for nonlinear estimation. In: Proceedings of the IEEE 2000 Adaptive Systems for Signal Processing, Communications, and Control Symposium. Lake Louise, AB, Canada (2000)

How to cite this article: Yun, J., Anderson, D., Fioranelli, F.: Estimation of drone intention using trajectory frequency defined in radar's measurement phase planes. IET Radar Sonar Navig. 17(9), 1327–1341 (2023). https://doi.org/10.1049/rsn2.12422

APPENDIX A

Tracking Filter Equations

To estimate the output vector, the state vector of the tracking filter, $\mathbf{x}$, is defined by

$$\mathbf{x} = \begin{bmatrix} \mathbf{R}_{\text{rdr}}^{\intercal} & \mathbf{V}^{\intercal} \end{bmatrix}^{\intercal}, \tag{20}$$

where $\mathbf{R}_{\text{rdr}} = \begin{bmatrix} R_{x,\text{rdr}} & R_{y,\text{rdr}} & R_{z,\text{rdr}} \end{bmatrix}^{\intercal}$ is the relative position vector between the radar and the drone, and $\mathbf{V} = \begin{bmatrix} V_x & V_y & V_z \end{bmatrix}^{\intercal}$ is the velocity vector of the drone.

Assuming that the targets' manoeuvre can be modelled by the nearly constant velocity model [25], the state equation can be defined as

$$\dot{\mathbf{x}} = \begin{bmatrix} \mathbf{V}^{\intercal} & \mathbf{w}^{\intercal} \end{bmatrix}^{\intercal}, \tag{21}$$

where the process noise vector $\mathbf{w} = \begin{bmatrix} w_{V_x} & w_{V_y} & w_{V_z} \end{bmatrix}^{\intercal}$ is modelled as a Gaussian white noise acceleration.

The measurement vector with additive noise, $\hat{\mathbf{z}}$, is defined by

$$\begin{aligned} \hat{\mathbf{z}} &= \begin{bmatrix} \hat{R}_{\text{rdr}} & \hat{V}_{r,\text{rdr}} & \hat{A}_{\text{rdr}} & \hat{E}_{\text{rdr}} \end{bmatrix}^{\intercal} \\ &= \mathbf{z} + \mathbf{n}, \end{aligned} \tag{22}$$

where $\mathbf{n} = \begin{bmatrix} n_R & n_{V_r} & n_A & n_E \end{bmatrix}^{\intercal}$ is the Gaussian noise vector with a standard deviation vector $\boldsymbol{\sigma} = \begin{bmatrix} \sigma_R & \sigma_{V_r} & \sigma_A & \sigma_E \end{bmatrix}^{\intercal}$. Using the state variables defined in (20), the measurement equation is given as

$$\hat{R}_{\text{rdr}} = |\mathbf{R}_{\text{rdr}}| + n_R \tag{23}$$

$$\hat{V}_{r,\text{rdr}} = -\frac{(\mathbf{R}_{\text{rdr}} \cdot \mathbf{V})}{|\mathbf{R}_{\text{rdr}}|} + n_{V_r} \tag{24}$$

$$\hat{A}_{\text{rdr}} = \text{atan2}\left(R_{x,\text{rdr}}, R_{y,\text{rdr}}\right) + n_A \tag{25}$$

$$\hat{E}_{\text{rdr}} = \text{atan2}\left(R_{z,\text{rdr}}, \sqrt{R_{x,\text{rdr}}^2 + R_{y,\text{rdr}}^2}\right) + n_E. \tag{26}$$

As the measurement equation is nonlinear, the Unscented Kalman filter (UKF) [26] was adopted as a filtering algorithm.

For every update period of the tracking filter, the state vector, $\mathbf{x}$, is estimated based on the UKF algorithm. $\hat{\mathbf{x}}$ denotes the estimated state vector, and $\hat{\mathbf{y}}$ denotes the output vector which is computed using the estimated state variables, $\hat{\mathbf{x}}$. That is,

$$\hat{\mathbf{x}} = \begin{bmatrix} \hat{\mathbf{R}}_{\text{rdr}}^{\intercal} & \hat{\mathbf{V}}^{\intercal} \end{bmatrix}^{\intercal}, \tag{27}$$

and

$$\hat{\mathbf{y}} = \begin{bmatrix} \hat{R}_{\text{ast}} & \hat{E}_{\text{ast}} & \hat{V}_{r,\text{ast}} & \hat{V}_v \end{bmatrix}^{\intercal}, \tag{28}$$

where

$$\hat{R}_{\text{ast}} = |\hat{\mathbf{R}}_{\text{ast}}| \tag{29}$$

$$\hat{E}_{\text{ast}} = \text{atan2}\left(\hat{R}_{z,\text{ast}}, \sqrt{\hat{R}_{x,\text{ast}}^2 + \hat{R}_{y,\text{ast}}^2}\right) \tag{30}$$

$$\hat{V}_{r,\text{ast}} = -\frac{(\hat{\mathbf{R}}_{\text{ast}} \cdot \hat{\mathbf{V}})}{|\hat{\mathbf{R}}_{\text{ast}}|} \tag{31}$$

$$\hat{V}_v = \hat{V}_z. \tag{32}$$

$\hat{\mathbf{R}}_{\text{ast}}$ is the relative position vector between the asset and the drone, and it can be given as

$$\hat{\mathbf{R}}_{\text{ast}} = \hat{\mathbf{R}}_{\text{rdr}} - \mathbf{R}_{\text{rdr}}^{\text{ast}}, \tag{33}$$

where the relative position vector between the radar and the asset, $\mathbf{R}_{\text{rdr}}^{\text{ast}}$, is assumed to be known.

https://dspace.org/

Estimation of drone intention using trajectory frequency defined in radar's measurement phase planes

Yun, Joongsup; Anderson, David; Fioranelli, Francesco

2023-09-01
Institution of Engineering and Technology (IET)
https://doi.org/10.1049/rsn2.12422
Yun J, Anderson D, Fioranelli F. (2023) Estimation of drone intention using trajectory frequency defined in radar's measurement phase planes. IET Radar Sonar and Navigation, Volume 17, Issue 9, September 2023, pp. 1327-1341

Downloaded from a DSpace repository. https://dspace.org/